Astronomy & Astrophysics manuscript no. stellina_ref2
August 12, 2016
©ESO 2016

arXiv:1608.03455v1 [astro-ph.SR] 11 Aug 2016

Does the chemical signature of TYC 8442−1036−1 originate from a rotating massive star that died in a faint explosion?⋆

G. Cescutti[1,2] ⋆⋆, M. Valentini[3], P. François[4,5], C. Chiappini[3], E. Depagne[6], N. Christlieb[7], and C. Cortés[8,9]

[1] Centre for Astrophysics Research, School of Physics, Astronomy and Mathematics, University of Hertfordshire, College Lane, Hatfield AL10 9AB, UK
[2] BRIDGCE UK Network (www.bridgce.net), UK
[3] Leibniz-Institut für Astrophysik Potsdam (AIP), An der Sternwarte 16, 14482, Potsdam, Germany
[4] GEPI - Observatoire de Paris, 64 avenue de l'Observatoire, 75014, Paris, France
[5] Université de Picardie Jules Verne, 33 rue St-Leu, 80080 Amiens, France
[6] South African Astronomical Observatory (SAAO), Observatory Road Observatory Cape Town, WC 7925, South Africa
[7] Zentrum für Astronomie der Universität Heidelberg, Landessternwarte, Königstuhl 12, 69117 Heidelberg, Germany
[8] Departamento de Física, Facultad de Ciencias Básicas, Universidad Metropolitana de la Educación, Av. José Pedro Alessandri 774, 7760197 Nuñoa, Santiago, Chile
[9] Millennium Institute of Astrophysics (MAS), Santiago, Chile

Received xxxx / Accepted xxxx

ABSTRACT

Context. We have recently investigated the origin of chemical signatures observed in Galactic halo stars by means of a stochastic chemical evolution model. We have found that rotating massive stars are a promising way to explain several signatures observed in these fossil stars.
Aims. In the present paper we discuss how the extremely metal-poor halo star TYC 8442−1036−1, for which we have now obtained detailed abundances from VLT-UVES spectra, fits into the framework of our previous work.
Methods. We apply a standard 1D LTE analysis to the spectrum of this star. We measure the abundances of 14 chemical elements; for Na, Mg, Ca, Sc, Ti, V, Cr, Mn, Fe, Ni and Zn we compute the abundances using equivalent widths; for C, Sr and Ba we obtain the abundances by means of synthetic spectra generated by MOOG.
Results. We find an abundance of [Fe/H]= −3.5 ±0.13 dex based on our high resolution spectrum; this points to an iron content lower by a factor of three (0.5 dex) compared to the one obtained by a low resolution spectrum. The star has a [C/Fe] = 0.4 dex, and it is not carbon enhanced like most of the stars at this metallicity. Moreover, this star lies in the plane [Ba/Fe] vs. [Fe/H] in a relatively unusual position, shared by a few others galactic halo stars that is only marginally explained by our past results.
Conclusions. The comparison of the model results with the chemical abundance characteristics of this group of stars can be improved if we consider in our model the presence of faint supernovae coupled with rotating massive stars. These results seem to imply that rotating massive stars and faint supernovae scenarios are complementary to each other, and are both required in order to match the observed chemistry of the earliest phases of the chemical enrichment of the Universe.

Key words. Galaxy: evolution – Galaxy: halo – stars: abundances – stars: massive – stars: rotation – nuclear reactions, nucleosynthesis, abundances

1. Introduction

The study of extremely metal-poor (EMP) stars is of fundamental importance to reveal the nucleosynthesis production of the first stars and how they formed, and more in general they can be of high value to understand the behaviour of all massive stars. Therefore, the last 20 years have seen incredible efforts by observers worldwide to measure these elusive, far and faint objects in the Galactic halo, from the pioneering studies of McWilliam et al. (1995) and Ryan et al. (1996) to a new generation of data with 8m telescopes as e.g. in Cayrel et al. (2004) and Aoki et al. (2005), to the most recent works e.g. by Yong et al. (2013) and Roederer et al. (2014b).

In our recent work, we have provided an interpretation to the presence in EMP stars of specific chemical signatures by means of stochastic chemical evolution models. Our results supported the scenario in which the first stars that exploded and polluted the pristine interstellar medium (ISM) were rotating faster than the present day massive stars. Stellar evolution codes coupled with nuclear reaction chains have shown that this rotation produces mixing in the interior of the stars. This mixing impacts the nucleosynthesis of light elements such as carbon, nitrogen and oxygen (Hirschi 2007; Meynet et al. 2006) and it also predicts the production of s-process elements (Pignatari et al. 2008; Frischknecht et al. 2012, 2016). In this scenario in which the stars were fast rotating, chemical evolution models were able to explain several chemical anomalies observed in the early Universe: the almost Solar ratio of [N/O] and the increase and the spread in the [C/O] ratio (Chiappini et al. 2006), the low $^{12}C/^{13}C$ ratios (Chiappini et al. 2008), the spread present in the [C/O] and in the [N/O] ratios (Cescutti & Chiappini 2010), the primary evolution of Be and B (Prantzos 2012), the spread between light and heavy neutron capture elements (Cescutti et al. 2013).

⋆ Based on observations made with the ESO Very Large Telescope at Paranal Observatory, Chile (ID 094.B-0781(A); P.I. G. Cescutti).
⋆⋆ email to: g.cescutti@herts.ac.uk

In Cescutti & Chiappini (2014), we also predicted that in this scenario, EMP stars with a supersolar [Sr/Ba] ratio were expected to have a barium manly composed by even isotopes, clear signature of an s-process pollution by fast rotating massive stars. The observations that we present here, were granted in the context of the ESO proposal "Probing the sources of synthesis of neutron capture elements: Isotopic ratios of barium in halo stars", meant to verify this thesis. However, the metal-poor halo stars TYC 8442−1036−1 was a back-up target and it was selected on the criterium to be an (extremely) metal-poor star in the correct position in the sky, never observed with high-resolution spectroscopy and was observed due to bad weather conditions that prevented us to observe our main targets. TYC 8442−1036−1 was not a striking case among the 1777 bright (9 < B < 14) metal-poor candidates selected from the Hamburg/ESO Survey (HE 2220−4840) by Frebel et al. (2006). Its iron content measured from analyses of medium-resolution follow-up spectroscopy was [Fe/H]= −2.91 dex, quite low but not so impressing in a survey that managed to find HE 1327−2326 - the most iron-poor star for almost a decade (Frebel et al. 2005), only recently replaced in this record by SMSS J031300.36−670839.3 (Keller et al. 2014).

Nevertheless, our detailed abundance analysis presents surprises, among which the star is more metal-poor that what expected by the medium resolution results. The star presents also a [C/Fe] = 0.4 dex and therefore is not a carbon enhanced star, like most of the stars at this metallicity (Placco et al. 2014); actually, it looks more like a normal star similar to others studied by the First Stars collaboration (Cayrel et al. 2004; Spite et al. 2005, 2006). TYC 8442−1036−1 shows also chemical characteristics in the [Ba/Fe] vs [Fe/H] space that are just at the edge of predictions for our best model results in Cescutti & Chiappini (2014). The case of TYC 8442−1036−1 is relative rare but not unique, in fact about other 20 stars are just marginally consistent with our previous modelling; moreover, few other stars (∼2−3) cannot be explained by our model. Among the uncertainties of this model, there is the scenario of the r-process events, which is the magneto-rotationally driven scenario in Cescutti & Chiappini (2014). However, a similar outcome is obtained by assuming different scenarios for the r-process events, as in Cescutti et al. (2013) by adopting the electron-capture scenario and in Cescutti et al. (2015) by adopting the neutron stars merger scenario.

In the recent years, another scenario has been investigated to explain the characteristics of the EMP (and ultra metal-poor stars) of the halo. This new scenario does not refer to characteristics of the stars during their lives, but rather on their explosions (Cooke & Madau 2014). In fact, they investigate the impact of a variations in the explosion energy of the primordial SNe, as suggested by Tominaga et al. (2007) in the scenario of the faint SNe. The faint SNe produce less Fe compared to normal SNe and impacting in the results of a stochastic chemical evolution model for the early Universe. We decide to investigate in this paper also this scenario to see the impact to the neutron capture elements, not considered in the previous studies, and to compare its results to the results provided by the scenario of rotating massive stars. Moreover, the different explosion energy does not impact the production of the studied chemical elements determined by fast rotation. Therefore, the two scenario can be complementary and we will show results in which the two scenarios are coupled; these results can represent a solution to the class of objects with chemical characteristics similar to TYC 8442−1036−1.

2. Observations and data reduction

The observations were performed using UVES high-resolution spectrograph (Dekker et al. 2000) in slit mode, mounted at the UT2 Kueyen Telescope at the ESO Paranal Observatory (Chile). We adopted the standard R530 setup (Red Arm only, Cross Disperser 3 and centered at 520 nm), covering the wavelength interval 4140–6210 Å, with a resolving power of R ∼100,000.

The spectrum was acquired on the night of 4th October 2014, adopting an exposure time of 20 minutes. The resulting spectrum has an average SNR of 100 (from 80 at 4200 Å to 150 at $\lambda > 5500$ Å). Details of the observation are summarised in Table 1.

The spectrum was reduced using the ESO standard pipeline for UVES. The radial velocity (RV) was measured from the H-β line. The RV correction was applied using the standard IRAF package *RVcorrect*. The correction was confirmed by the subsequent comparison with the wavelengths of Fe and Ca lines.

3. Atmospheric parameters and abundances

We use stellar model atmospheres interpolated from the grid of one-dimensional MARCS models (Gustafsson et al. 2008) and performed the analysis using a recent version of the spectral line analysis code MOOG [1] . Effective temperatures ($T_{\rm eff}$) and microturbulent velocities (ξ_t) are derived by requiring that abundances derived from Fe I lines showed no trend with the excitation potential and line strength. The log(g) is derived by requiring that the Fe abundance derived from Fe I lines matched that derived from Fe II lines. This analysis technique is a standard analysis and very similar to the one adopted in Roederer et al. (2014a). Our calculations assume local thermodynamical equilibrium (LTE). The reference Solar abundances used in this work are taken from Asplund et al. (2009).

The line list adopted in this work has been created starting from the line adopted in Hill et al. (2002), Roederer (2013) and Ural et al. (2015) supplemented by lines taken directly from VALD3 (Kupka et al. 2000). The line list was constructed in order to avoid as much as possible blends with other atomic lines and molecular bands. The EW of the lines have been measured using the ARES (Automatic Routine for line Equivalent widths in stellar Spectra; Sousa et al. 2007). In Table .1, we report the wavelengths, excitation energy of the lower energy level, oscillator strength and EW for the considered lines. A fraction of the considered lines has been measured using standard IRAF routine: no bias or significative differences between the automatically measured EWs and the ones determined with the automatic routine have been detected. The final atmospheric parameters derived are $T_{\rm eff}$ = 4800K, log(g) = 1.71 dex and [Fe/H]= −3.50 dex with ξ_t = 1.71 km s^{-1}.

For some abundances in Table 2 the standard variation (σ_ϵ, column 5) involving small numbers of lines (column 6) is implausibly small. Therefore, for the abundances measured with less than five lines we assume as random error (column 7) the largest standard variation obtained for the remaining abundances (0.11 dex for Fe II). The total error is obtained by quadratically adding this updated random error with the systematic error. To calculate the systematic errors, we have re-computed the abundances, varying the model atmosphere considering these uncertainties: Δ $T_{eff}\pm$ 100K, Δ log(g) ± 0.3 dex, Δ [Fe/H] ±0.3 dex and Δ ξ_t ± 0.3 km s^{-1}. This method to calculate the systematic errors and the uncertainties adopted are based on the recent

[1] http://www.as.utexas.edu/~chris/moog.html

Table 1. Observing log

Object	R.A. (J2000.0)	Decl. (J2000.0)	B (mag)	V (mag)	Exposure time (s)	S/N	Obs. Date (UT)	V_r (kms^{-1})	error (kms^{-1})
TYC 8442−1036−1	22 23 23.3	-48 24 50.9	11.71	11.10	1200s	>80	4th October 2014	90.6	0.6

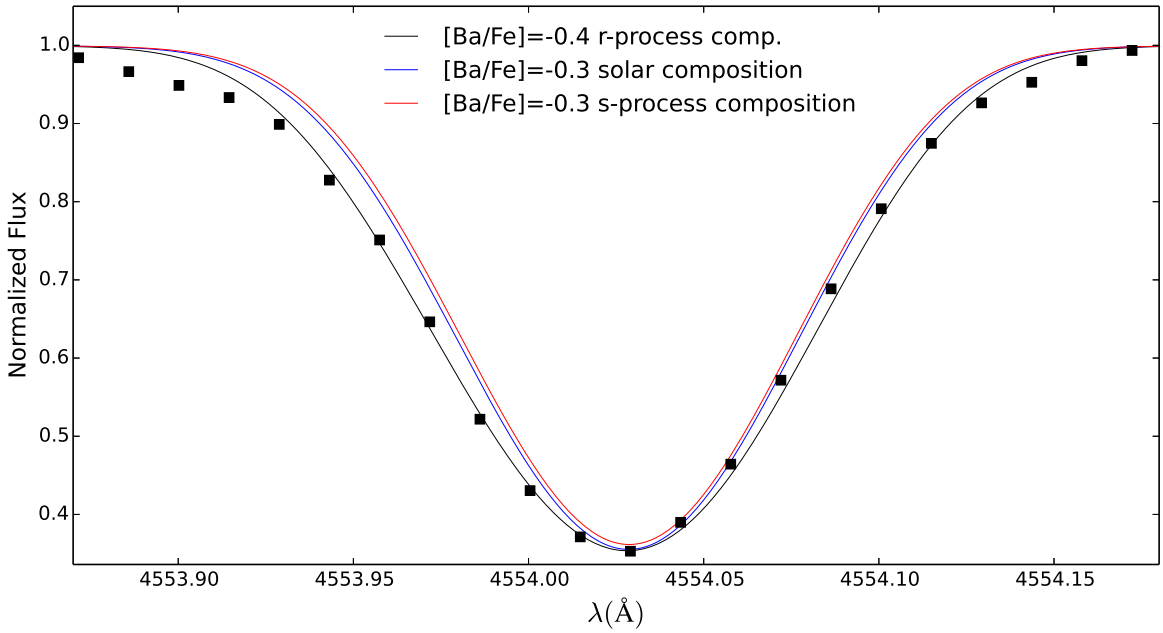

Fig. 1. Fit of the Ba line at 4554 Å. The observed spectrum are represented by dots, the synthetic spectra by lines. We present the different results obtained using different isotopic compositions for Ba: r-process composition, s-process composition and solar composition. Note that we have obtained different best abundances for the different compositions.

Table 2. Abundances of chemical elements in TYC 8442−1036−1. For the abundance values in column 4, we use the Solar abundances by Asplund et al. (2009).

chemical elements	$\epsilon(X)$	[X/H]	[X/Fe]	$\sigma_{\epsilon(x)}$	N. lines	random error	systematic error	total error	corrections non-LTE
C (CH)	5.33	−3.10	0.4	–	synth	(0.20)	(0.12)	0.23	-
Na I	2.48	−3.76	−0.26	0.01	2	0.11	0.03	0.11	−0.06
Mg I	4.73	−2.88	0.62	0.05	3	0.11	0.01	0.11	0.10
Ca I	3.14	−3.20	0.30	0.07	11	0.07	0.05	0.08	-
Sc II	−0.27	−3.42	0.08	0.06	6	0.06	0.11	0.12	-
Ti I	1.67	−3.27	0.23	0.07	8	0.07	0.03	0.08	-
Ti II	1.65	−3.29	0.21	0.10	23	0.10	0.12	0.15	-
V I	0.42	−3.51	−0.01	–	1	0.11	0.04	0.12	-
Cr I	1.63	−4.01	−0.51	0.09	4	0.11	0.03	0.11	-
Mn I	1.79	−3.64	−0.14	0.07	2	0.11	0.03	0.11	-
Fe I	4.00	−3.50	–	0.06	86	0.06	0.11	0.13	0.10
Fe II	4.00	−3.50	–	0.11	11	0.11	0.09	0.14	-
Ni I	3.03	−3.19	0.31	–	1	0.11	0.04	0.12	-
Zn I	1.36	−3.20	0.30	0.09	2	0.11	0.05	0.12	-
Sr II	−1.43	−4.30	−0.80	–	synth	(0.20)	(0.12)	0.23	-
Ba II	−1.72	−3.90	−0.40	–	synth	(0.20)	(0.12)	0.23	-

work on EMP halo stars by Yong et al. (2013); however similar method and values are used also in the work by Roederer et al. (2014a). The quadratic sum of these variations is reported in Table 2.

We underline that the analysis performed in this work was made under the assumption of 1D LTE. Assuming LTE, means to imply that the energy distribution is performed only by particles collision. This assumption stops to be true close to the stellar surface (Bergemann & Nordlander 2014). TYC 8442−1036−1 is a giant and extremely metal poor star and the non-LTE effects can be important in particular for Na, Mg and Fe. In Table 2, we report non-LTE corrections for these elements taken from literature, to give the reader an indication of the expected non-LTE effects. We find a variation up to +0.10 for Mg on two

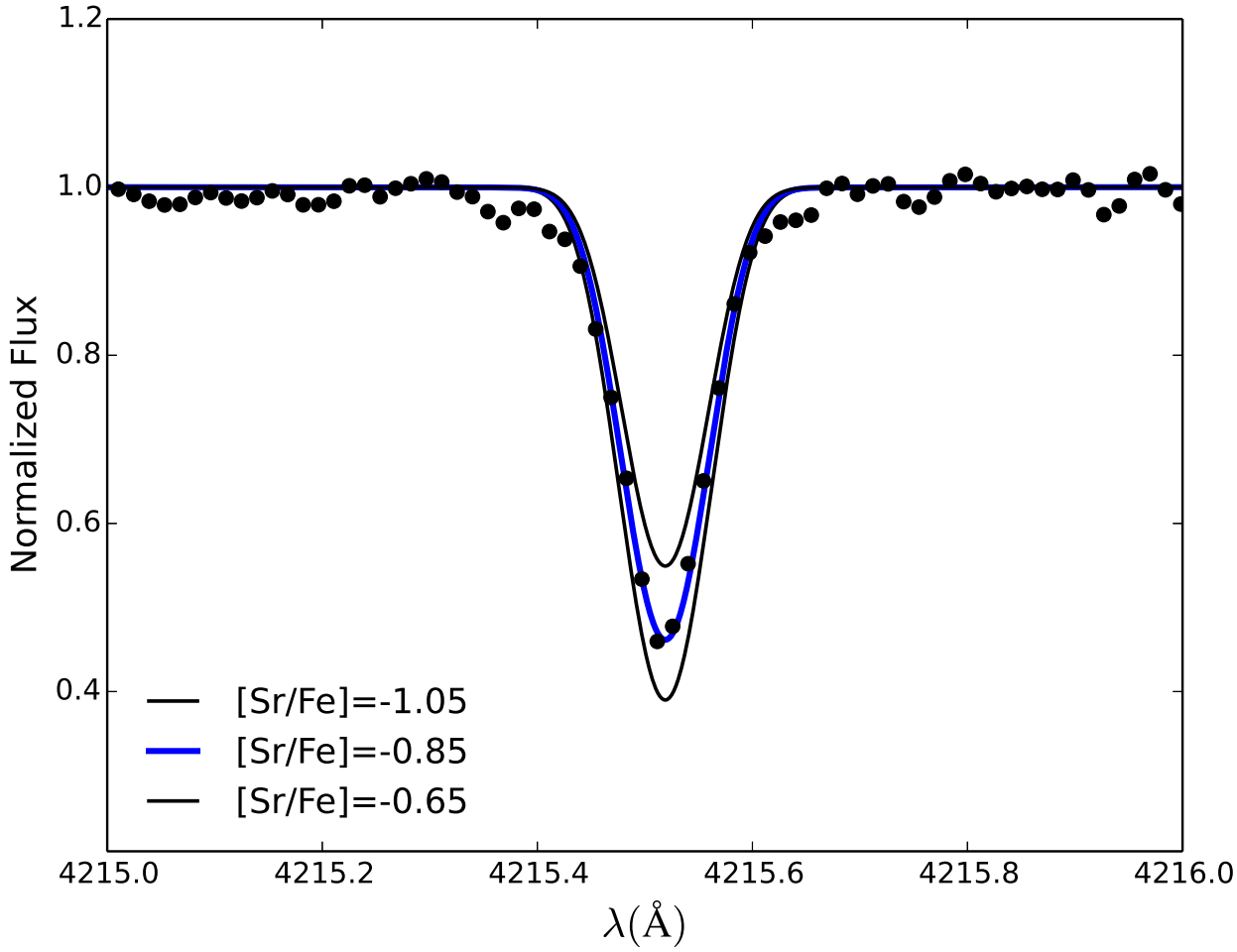

Fig. 2. Fit of the Sr line at 4607 Å. Dots: observed spectrum, lines synthetic spectra. The synthetic spectra are calculated for 3 different abundances of Sr. The intermediate one has been taken as best value for the Sr abundance measured in this star.

of the three lines considered here (see Osorio & Barklem 2016). However, following Merle et al. (2011), the corrections for Mg abundance are +0.19 dex for the line at 4703Å and 0.25 dex for the one at 5528 Å. An intermediate results is obtained with the corrections by Mashonkina (2013). We also note that we do not take into account the line at 4571Å for which the correction could have been higher (up to 0.3 dex). For an estime of the non-LTE correction of Na, we provide the corrections calculated by the online database INSPECT [2]; the corrections for Na in this database are from Lind et al. (2011). Finally, we expect a non-LTE corrections for our Fe I of 0.1 dex (0.2 dex at maximum), based on Lind et al. (2012). The abundance of Fe II is expected to be not affected by the non-LTE corrections and its value is still compatible with the estimate value of Fe I with non-LTE corrections. The corrections for non-LTE effect can be important for Mn and Cr (Bergemann & Gehren 2008; Bergemann & Cescutti 2010); however, concerning Mn, recent results obtained by Sneden et al. (2015) can challenge the impact of non-LTE corrections. In Sect. 6 we present figures with the abundances of TYC 8442−1036−1 and other observational data taken from literature. In these figures, we use the abundances without non-LTE corrections, since considering these corrections will not alter our conclusions and most of the other data do not consider these corrections.

Abundances of C, Sr and Ba are derived using the spectral synthesis module of MOOG. The abundances of the elements are iteratively varied until the synthetic spectrum matched the observed one by visual inspection. The macro-turbulent broadening is determined using a Gaussian representing the combined effects of the instrumental profile, atmospheric turbulence, and stellar rotation. The width of this Gaussian is estimated during the spectrum synthesis fitting, and the abundances are thus (slightly) sensitive to the adopted broadening. The lines of Ba II are affected by hyperfine splitting and also by isotopic splitting. Therefore, the Ba abundances are computed assuming the McWilliam (1998) r-process isotopic composition and hyperfine splitting. We compare in Fig. 1 the differences arising in the shape of the synthetic line of Ba at 4554 Å when two different isotopic compositions are adopted: a solar compositions and a typical s-process composition. We note that the final abundance obtained from the lines 4554 Å and 4914 Å are about 0.4 dex lower taking the hyperfine splitting and isotopic splitting into account. On the contrary, the abundance calculated on the lines 6110 Å and 5883 Å are in good agreement with the abundances measured from their EWs. This was expected, given the lower

[2] http://inspect.coolstars19.com, A database for Interactive NLTE Spectroscopy of late-type stars.

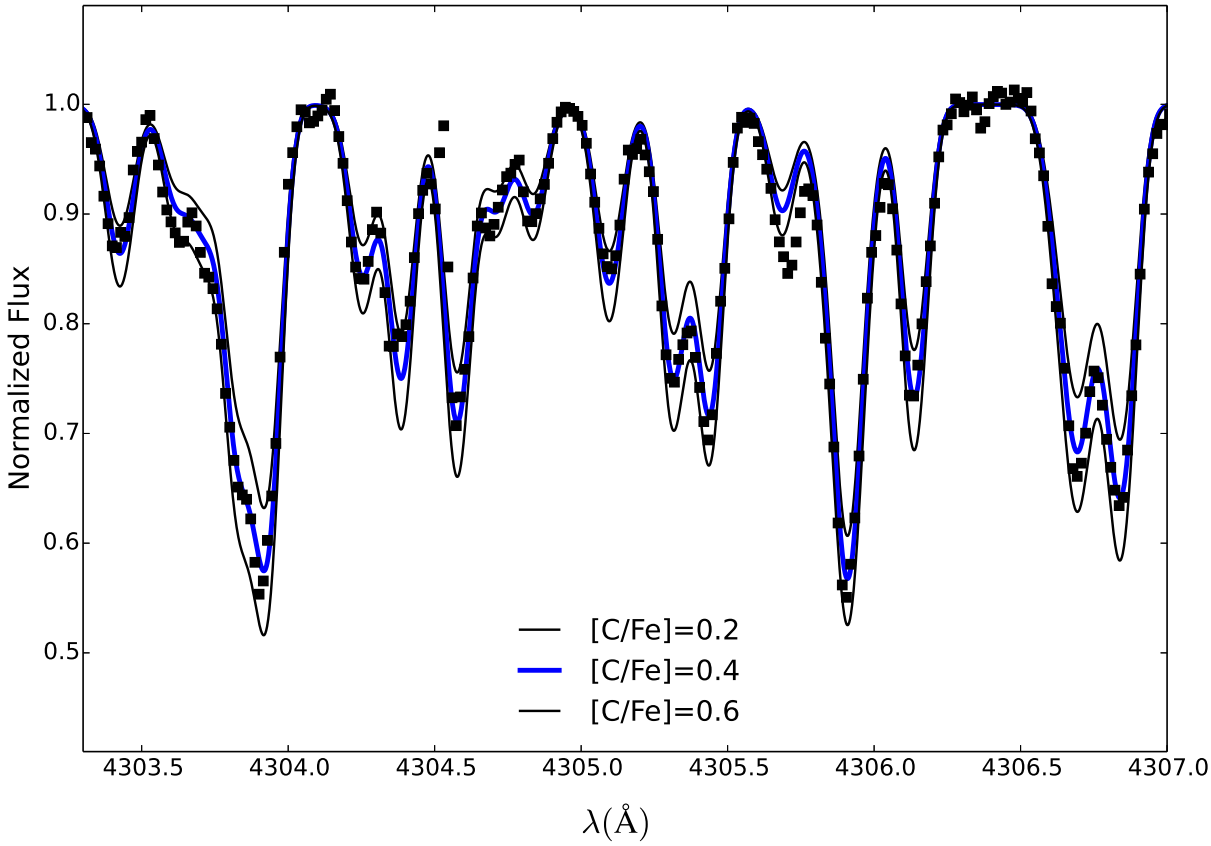

Fig. 3. Fit of CH lines of the G band in TYC 8442−1036−1. Dots: observations, lines: synthetic spectra computed for the abundances indicated

impact of the splitting in the latter lines. Also for the measurement of Sr abundance we decide to use the synthetic analysis (see Fig. 2). The C abundance was measured in a similar way from analysis of the band of the A−X electronic transitions of the CH molecule. Fig. 3 shows a comparison of the synthetic spectrum with the data in the range 4303–4307 Å. The random abundance errors obtained with synthetic spectra (C, Sr and Ba) are assumed to be 0.2 dex; in fact, for the three analysed elements the observed spectrum is inside this variation of the synthetic spectrum (see Fig. 2 and 3) We also assume for the systematic errors of these abundance 0.12 dex, the maximum systematic error computed among the other elements, for a total error of 0.23 dex.

4. Chemical evolution model

The chemical evolution model used is the same as in Cescutti & Chiappini (2014), which is based on the stochastic model developed in Cescutti (2008), but with a different treatment of the gas flows, following the homogeneous model of Chiappini et al. (2008). The halo is assumed to consist of many independent regions, each with the same typical volume, and each region does not interact with the others. Accordingly, the dimensions of the volume are expected to be large enough to allow us to neglect the interactions between different volumes, at least as a first approximation. For typical ISM densities, a supernova remnant becomes indistinguishable from the ISM – that is, it merges with the ISM – before reaching ∼ 50 pc (Thornton et al. 1998); therefore, we decided to have a typical volume with a radius of roughly 90 pc. The dimension of this volume is the same as in our previous works adopting a stochastic model for the Galactic halo (Cescutti 2008; Cescutti & Chiappini 2010; Cescutti et al. 2013; Cescutti & Chiappini 2014; Cescutti et al. 2015). The number of assumed volumes to ensure a good statistics in our previous models was 100; however given the variation we implement here for the iron yields (see next section), the new models are based on the results of 1000 volumes. We did not use larger volumes because they would produce more homogeneous results; in fact, in larger volumes the model would predict more SNe events and a mixture of enrichments that would decrease the maximum spread possible for the set of yields used. Knowing the mass that is transformed into stars in a time step (hereafter, M^{new}_{stars}), we assigned the mass to one star with a random function, weighted according to the initial mass function (IMF) of Scalo (1986) in the range between 0.1 and 100 $M_{\odot}$. We then extracted the mass of another star and repeated this cycle until the total mass of newly formed stars exceeded M^{new}_{stars}. In this way, M^{new}_{stars} is the same in each region at each time step, but the total number and mass distribution of the stars are different. We thus know the mass of each star contained in each region, when it is born and when it will die, assuming the stellar lifetimes of Maeder & Meynet (1989). At the end of its lifetime, each star enriches the ISM with its newly produced chemical elements and with the elements locked in that star when it was formed, excluding the fractions of the elements that are permanently locked in to the remnant. As shown in Cescutti et al. (2013), our model is able to reproduce the MDF measured for the halo by Li et al. (2010). This comparison shows that the timescale of enrichment

of the model is compatible with that of the halo stars in the Solar vicinity. Moreover, our model predicts a small spread for the α-elements Ca and Si, which is compatible with the observational data.

5. Modelling the nucleosynthesis

5.1. Stellar yields for Fe

Our goal is to explore the impact on the chemical evolution model of the scenario in which massive stars do not always explode as SNe II with a standard energy of 10^{51}erg, but they also explode with fainter explosions, as observationally motivated by Moriya et al. (2010).

At the present, the mechanism of explosion of SNe II in not fully understood (see Janka et al. 2012) as well as possible connection between mass and explosion energy for a SNe. Therefore, in the nucleosynthesis results, the explosions are not obtained from first principles, and they must be tuned in some way, typically given final kinetic energy of the ejecta or a given amount of Fe ejected (see Chieffi & Limongi 2013; Woosley & Weaver 1995; Nomoto et al. 2006).

In our model rather than stochastically select an explosion energy and calculate the Fe ejected, we vary directly the Fe ejected. In particular, we decide to assume for the production of iron in massive stars ($8 - 80 M_{\odot}$) a distribution of yields which goes from almost zero - $10^{-5} M_{\odot}$ in the case of the faintest explosions - to 0.2 $M_{\odot}$. In this range, any value has the same probability to be randomly chosen, so on average a massive star enriches the ISM with 0.1 $M_{\odot}$ of iron; in this way, the mean chemical evolution of Fe is preserved.

These assumptions are crude, but given the complexity connected to the process of the explosion of a SNe II, we decide to keep our assumptions as simple as possible. With this hypothesis, we can check in our stochastic model the impact of the presence of a distribution of energies from faint SNe to normal SNe. In Sect. 6, we show for comparison the results obtained in Cescutti & Chiappini (2014), with our standard assumptions for Fe: the solar metallicity yields of Woosley & Weaver (1995). In all models, we have considered the SNe Ia enrichment, as in Cescutti et al. (2006).

5.2. Stellar yields for C

For carbon, we present the results with two set of yields for the massive stars and low-intermediate mass stars. We have chosen these sets to visualize the difference between the carbon production in rotating and non-rotating stellar evolution models:

- *rotating yields*, the set of yields of the model a described in Cescutti & Chiappini (2010), based on the yields by Meynet & Maeder (2002) for z $\geq$ 10^{-5}, and on the total yields by Hirschi (2007) for z = 10^{-8}. For low-intermediate mass stars, we adopt the stellar yields by Meynet & Maeder (2002).
- *non-rotating yields*, the carbon yields calculated by Woosley & Weaver (1995), which is a set of yields frequently adopted in chemical evolution studies, but without rotation. For the low-intermediate mass stars we assume the yields by van den Hoek & Groenewegen (1997).

The two set of yields for carbon do not originate from the same group and/or stellar evolution code, so it is possible that also systematic effects produce differences between them and not only the rotation. Nevertheless, we confirm that yields from the Geneve group without rotation produce less carbon compared to the *rotating yields*, similarly to *non-rotating yields* assumed here.

Table 3. The nucleosynthesis prescriptions adopted for the 3 models.

Models Fig. 4, 5 & 6	yields for Fe	yields for Ba and C
spinstars scenario	standard	rotating
faint SNe scenario	with variance	non-rotating
spinning faint scenario	with variance	rotating

5.3. Stellar yields for Ba and Sr

For barium and strontium, we use for all the models with rotating massive stars the nucleosynthesis of the *MRD+s B2* model described in Cescutti & Chiappini (2014). These elements can be produced in this model by both the s-process and the r-process in massive stars. The assumed r-process scenario follows the idea described in Winteler et al. (2012) and recently confirmed by Nishimura et al. (2015), where a small percentage of massive stars end their lives as magneto-rotationally driven (MRD) SNe. To implement this scenario into our chemical evolution model, we randomly select 10% of all the simulated massive stars and we assume that these massive stars generate an r-process event at the end of their lives. We have no prediction of the ejected mass in each r-process event. On these grounds, we assume that the MRD scenario produces the same amount of Ba in a stellar generation as the EC+s model (Cescutti et al. 2013); these empirical yields were obtained as the simplest array able to reproduce the observed trend in Galactic halo star of increasing [Ba/Fe] with metallicity. In this scenario, we take also into account the possibility that the amount of r-process material ejected is not constant (for details on the variation see Cescutti & Chiappini 2014). The presence or absence of rotation does not influence the r-process production in our set of yields. The contribution by the s-process in rotating massive stars is assumed as in the *fs*-model of Cescutti et al. (2013), where we considered the stellar yields obtained by Frischknecht et al. (2012). The barium and strontium produced by the s-process is only barely affected by the SNe II explosion, and therefore it is relatively safe to consider a variation of iron without changing these yields. It may be not the case for the Ba r-process production, and we comment on this in the Section 6. In the non-rotating model there is no s-process production of Ba and Sr from rotating massive stars. However, in all the models, we consider the s-process contribution from stars in the mass range 1.3–3 $M_{\odot}$, by implementing the yields by Cristallo et al. (2009, 2011). We underline that this production channel affects the model results only at moderate metallicity ([Fe/H] ~ -1.5 dex).

6. Results

6.1. Results for Ba

In Fig. 4, we show the results of three models for [Ba/Fe] vs. [Fe/H]. Two models take into account rotating massive stars: one model considers the presence of faint SNe that can produce an almost negligible amount of iron ("spinning faint scenario"), in the other (contour plot with dashed line), the SNe II produce a fixed amount of iron (roughly 0.1 $M_{\odot}$), following the results by Woosley & Weaver (1995) ("spinstar scenario"). In the last model (contour plot with solid line), we consider non-rotating

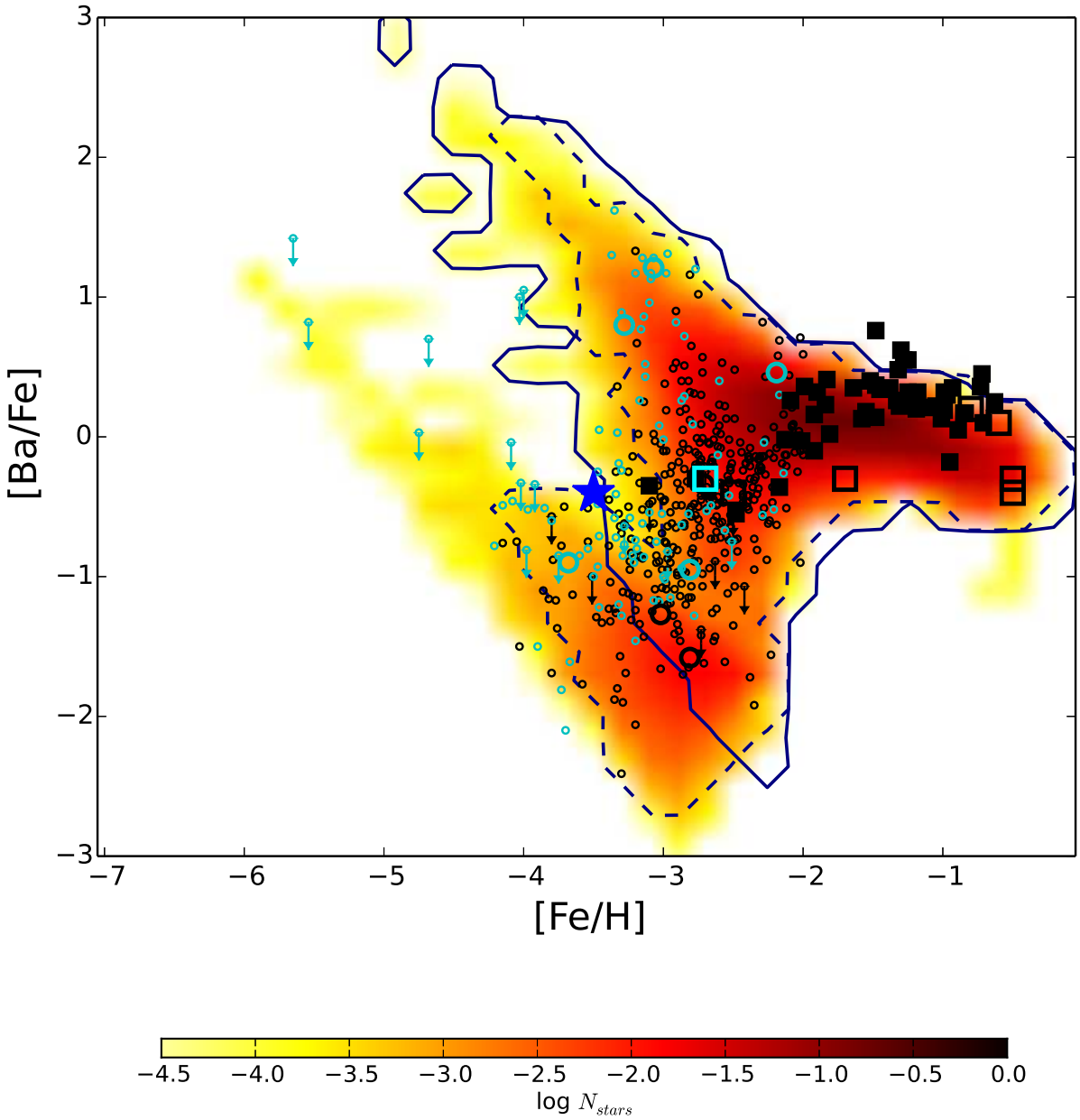

Fig. 4. [Ba/Fe] vs. [Fe/H]. The star analysed here is shown using a blue star; the open small dots are data collected by Placco et al. (2014) and the arrows indicate upper limits; the big open dots are data from Hansen et al. (2015b); the solid squares from Hansen et al. (2012); the open squares are taken from Hansen et al. (2015a). The cyan symbols refer to CEMP-no stars, adopting the criterion [C/Fe] > 0.7 condition for carbon enhancement, as in Placco et al. (2014); the black symbols are for normal star. We do not plot stars with s-process enhancement (CEMP-s). The color-coded surface density plot presents the density of long living stars for the model of spinning faint SNe. The contour plot with dashed line shows the results for the model of spinstars, the contour plot with solid line shows the results for the model of faint SNe.

massive stars and the presence of faint SNe ("faint SNe scenario"). The nucleosynthesis yields are summarised in Table 3. We compare our models to the star analysed here and to a collection of observational data.

The "spinstars scenario" (that is the same model for Ba as the model "MDR+s B2" realised in Cescutti & Chiappini 2014) is quite successful, because in the space [Ba/Fe] vs. [Fe/H], the density of its simulated long-living stars is matching most of the stars observed in the halo. However, a certain number of objects at extremely low metallicity and low [Ba/Fe] are positioned where the model predicts a null density of stars. It was also unable to explain stars at [Fe/H] ~ -3.5 dex at [Ba/Fe] ~ -0.5 dex. In particular also the star we have characterised here is found in this area.

On the other hand, in Fig. 4, the results of the model "spinning faint scenario" explain, within the observational errors all the stars at [Fe/H] < -4 dex. It also simulates stars at [Fe/H] ~ -3.5 dex at [Ba/Fe] ~ -0.5 dex and compatible with the star analysed here. The density plot produced by this model shows two bands which move downwards from [Fe/H] ~ -6 dex to [Fe/H] ~ -3 dex. The band at lower [Ba/Fe] has been enriched by spinstars with an associated SNe II with a low iron production (faint SNe). Therefore, this coupling helps in better recovering the observed stars at the lowest [Fe/H], which are mostly in this lower band. The second band with low [Fe/H] but high [Ba/Fe] is produced in the model by r-process events coupled with weak production of iron. Stars in the region are not observed for [Fe/H] < -4 dex; if this absence will be confirmed by future observations, it will provide an additional contraint to the r-process events: they should be associated with a normal production of Fe, and not to faint SNe. This constraint applies in case of single massive stars as progenitors of the r-process

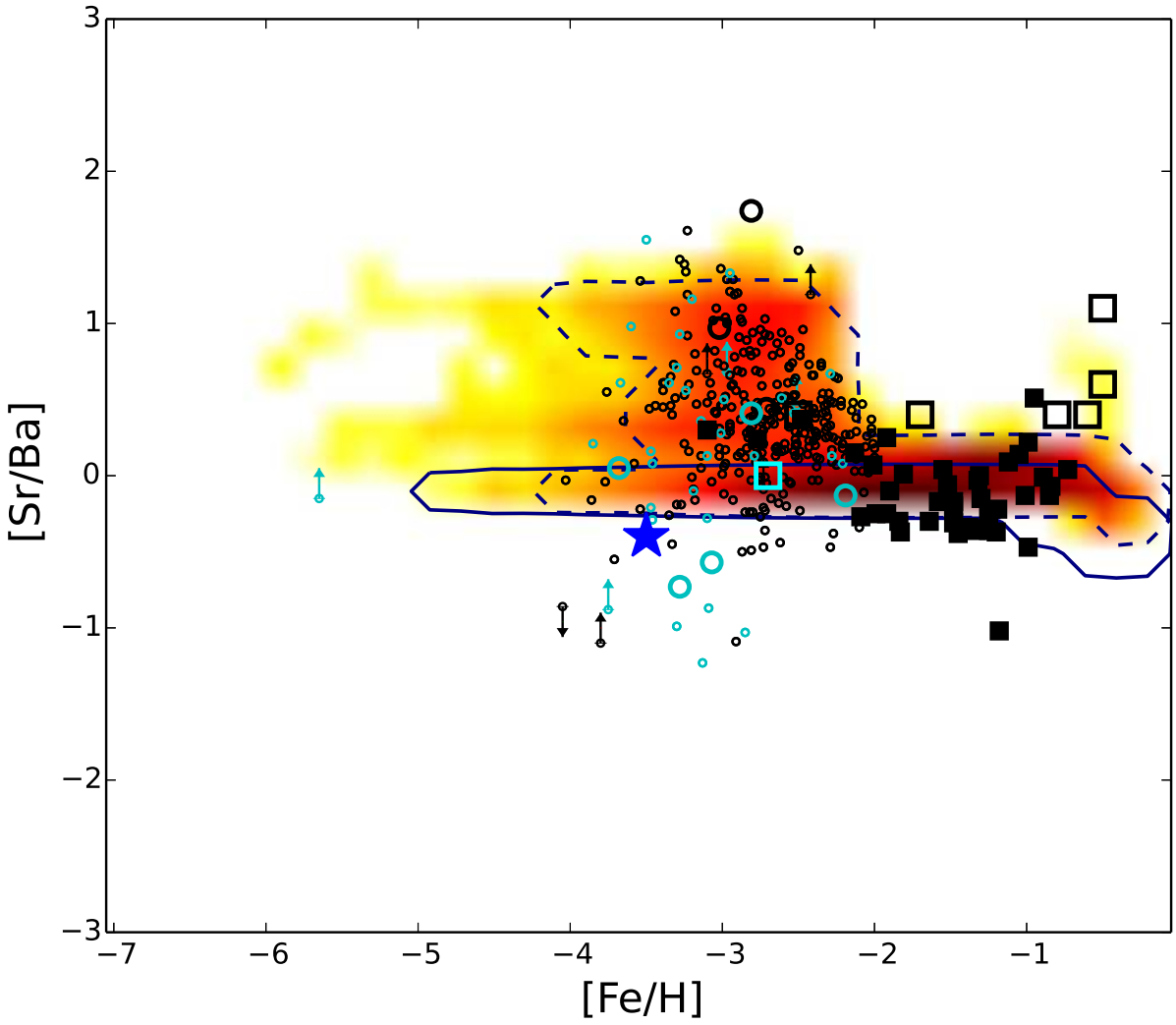

Fig. 5. [Sr/Ba] vs. [Fe/H]. The symbols are the same as in Fig. 4. The color-coded surface density plot and the contour plots describe the same models as in Fig. 4.

events, whereas in the case of neutron-stars merger scenario, it should be applied to at least one of the two massive progenitor stars.

In the model "faint SNe scenario", we do not consider production of s-process by massive stars. The results of this model are only marginally consistent with the abundances measured in TYC 8442−1036−1. Considering non-LTE corrections for our star will increase its agreement with the "faint SNe scenario"; however, this model still fails to reproduce the stars located in the band at lower [Ba/Fe] in the results of the "spinning faint scenario".

6.2. Results for [Sr/Ba]

We present in the Fig.5, the results of the three models for [Sr/Ba] vs. [Fe/H]. Similarly to the [Ba/Fe] case in the previous section, the"spinstars scenario" model is really successful, because in the space [Sr/Ba] vs. [Fe/H], the density of its simulated long-living stars can recover most of the stars observed in the halo. Still, a certain number of objects are located at extremely low metallicity where this model predicts a null density of stars. Again this issue is improved, once we adopted also a variation of yield for the iron, as in the case of of "spinning faint scenario" .

The Fig. 5 also explained why the spinstars s-process contribution is essential. Indeed the "faint SNe scenario" - without this contribution - cannot reproduce a large fraction of abundances observed in Galactic stars. We note that in this figure there is also fraction of stars that is compatible with none of the scenarios investigated here. These outliers are located below the [Sr/Ba] ratio assumed for the r-process events and cannot be reproduced, being also the s-process produced by the spinstars with a [Sr/Ba]>0. However, their fraction is small and in the [Sr/Ba] plot the errors of both chemical element abundances should be considered; therefore a substantial fraction of them is still compatible within the errors to the results and TYC 8442−1036−1 is in this group. Finally,the CEMP-no stars in this group could be originated in a binary system, therefore they show a mild enhancement due to the pollution of s-process material from the companion star. If this possible scenario is taken into account only two EMP stars are outliers compared to our models which is an excellent results.

6.3. Results for C

Going towards extremely low metallicity, an increasing fraction of stars are carbon-rich and belong to the category of the CEMP-no stars [3]. However, the star we have analysed does not belong to this category, being only slightly carbon enhanced. Therefore,

[3] In Beers & Christlieb (2005), a metal-poor star is a CEMP star if [C/Fe]>1. If there is no excess of s-process ([Ba/Fe]< 1) the star belongs to the CEMP-no category, otherwise to the CEMP-s class.

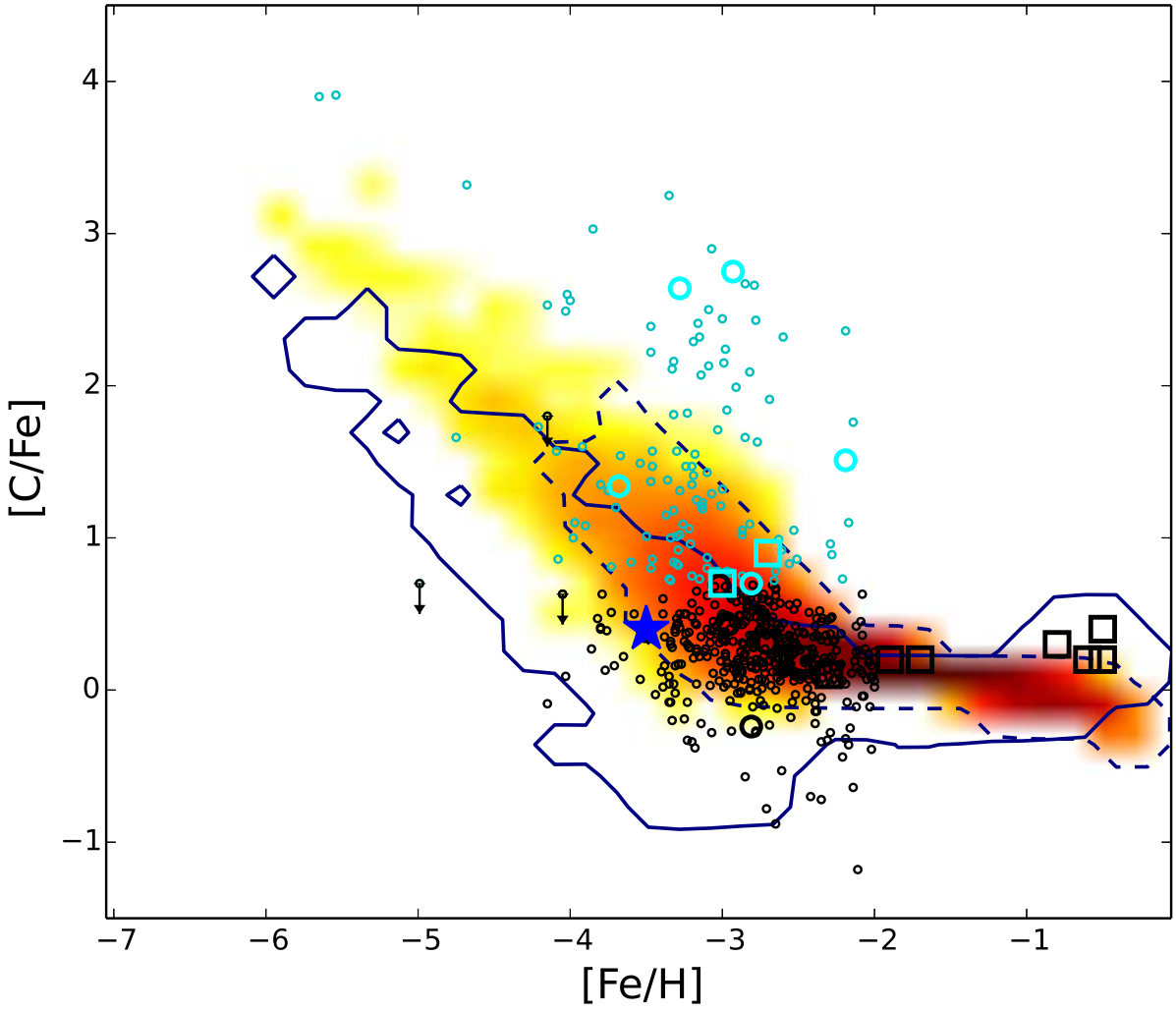

Fig. 6. [C/Fe] vs. [Fe/H]. The symbols are the same as in Fig. 4. The color-coded surface density plot and the contour plots describe the same models as in Fig. 4.

we decide to investigate how our spinning faint SNe model behaves in terms of [C/Fe] ratio vs. [Fe/H]. The results are shown in Fig. 6. In this figure again the density plot represents the results for the "spinning faint SNe scenario", whereas the contour plot with dashed line shows the results of the "spinstars scenario" where SNe II produce a fixed amount of iron. The solid line contour plot represents the results assuming non-rotating yields for carbon (see Table 3 for details), and in this model ("faint SNe scenario") we consider a variation in iron yields.

The low production of iron by faint SNe produces a rise in the [C/Fe] ratio towards low metallicity, and this trend is common in both models that consider faint SNe ("spinning faint SNe scenario" and "faint SNe scenario") with and without rotation. However, the model with rotation predicts a density distribution of stars with a [C/Fe] ratio about 1 dex higher compared to the non-rotating yields for [Fe/H] < -3 dex.

The higher production of carbon in the yields with rotation improve the agreement between the model and the data. In fact, a substantial number of Galactic stars is inside the predictions of the faint spinstars model for $-3 <$ [Fe/H]< -4 dex and [C/Fe]$\sim$1 dex, and outside the predictions of the model assuming yields without rotation. The chemical enrichment of the star measured here, is consistent with both rotation and non-rotational models. We also note that the model with rotation cannot explain a fraction of stars with lower ratio of [C/Fe] that are possible to be reproduced in the model without rotation. This could show a fact that is expected: a distribution of rotational velocities among the massive stars. We underline that it will be also possible in the near future to investigate the most likely distribution of stellar rotation for these low-metallicity massive stars with a set of nucleosynthesis computations where yields for different rotational velocity are provided. In comparison with the "spinning faint SNe scenario" the model with fixed amount of iron produced by SNe II ("spinstars scenario", dashed contour) cannot reproduce the data for [Fe/H]< -4 dex. Moreover, a not negligible fraction of stars is located just inside the upper edge of the contour for $-4<$[Fe/H]< -3, where the results of the model predict a very low density of long living stars; therefore the model is not fully consistent with the data.

The spinning faint SNe model cannot be considered an exhaustive explanation for the CEMP-no stars. A not negligible fraction of the observed CEMP-no stars present a [C/Fe] not compatible with the predictions of the model. The carbon present in these objects is in some case more than 1 dex compared to the spinning faint SNe model results. This class of objects has also been identified in Cooke & Madau (2014), and called "super CEMP".

It is likely that the carbon present (at least) in this class of CEMP-no stars was not well mixed in the ISM, before being locked in these low-mass stars. In Meynet et al. (2010), the chemical signatures present in the three most iron-poor stars

known (at that time), [4] which are also CEMP-no stars, were explained assuming that these stars were formed (almost) entirely by stellar winds of rotating massive stars. In this scenario the [C/Fe] of these stars can be strongly enhanced compared to the results of a standard chemical model, where the stellar enrichment is well mixed with the ISM before forming new stars. In our plots, these stars are present, they belong to the category of stars that lay above our model predictions and are the first three data points starting approximately at [Fe/H]= −6 dex. The presence of this class of "super CEMP", was already noted in Cescutti & Chiappini (2010), where we could not reconcile our models with a large fraction of the CEMP-no (known at that time). The issue was quite clear also in the [C/O] (and [N/O]) vs [O/H] space, where it was possible to neglect the influence of the uncertainties in the production of iron.

Recently, it was also underlined by Maeder & Meynet (2015) that different sub-classes of CEMP-no stars should be considered in the context of formation by stellar winds. They are probably determined by different degrees of internal mixing during stellar evolution. It will be possible to take all these differences into account only when models with nucleosynthesis covering a broad range of stellar masses, initial metallicities, and CNO ratios, rotational velocities, and mass loss rates will be available. Therefore, it is not surprising that in the context of a chemical evolution model, where only full mixing with the ISM is considered and just a grid of models for two velocities are available, we cannot fully explain all the CEMP-no stars.

Another possible explanation is that at least a fraction of these CEMP-no stars are the secondary in a binary system. In this scenario, the star presents the pristine composition polluted by AGB material of the primary star. This is the same scenario that is favorite for the CEMP-s, and in this case the absence of strong enrichment of barium can be explained in the framework of classical theoretical yields for AGB stars; the very low-metallicity reduces the barium production and enhances the production of the lead (Cristallo et al. 2011). It is also possible that the evolution of low-mass star is quite different at extremely-low metallicity and it can suppress the s-process production (Fujimoto et al. 2000; Komiya et al. 2007). As found in Cooke & Madau (2014), at least 3 out of 5 the stars of this group show evidence to be binary (Starkenburg et al. 2014); however, very recently Hansen et al. (2015b) found no compelling relation between binarity and carbon enhancement.

Given the complexity of the observational data, we have shown that the spinning faint SNe model has successfully recovered the main trend of the data. In fact, the star studied here and a substantial fraction of extremely metal-poor (CEMP-no and normal) stars can be formed in the framework of normal chemical evolution, if we couple the fast-rotating yields and the presence of faint SNe. Moreover, for elements that are not expected to be ejected by stellar winds, as Ba, we have shown that basically all the observational data available are compatible with the predictions of the spinning faint SNe model.

7. Conclusions

We have measured from a high-resolution spectrum 13 chemical elements for TYC 8442−1036−1, a metal-poor star of the Galactic halo. This star belongs to the rare class of EMP stars with [Fe/H] = −3.5±0.13 dex, 0.5 dex lower than what previously determined with a medium resolution spectrum. At this metallicity, most of the stars in the Galactic halo have a [C/Fe] > 0.7 dex and belong to the class of the CEMP-no stars. This is not the case for our star which shows just mild overabundance of carbon ([C/Fe] = 0.4 dex). We have also measured with particular attention its [Ba/Fe] ratio, and we find a low abundance of about [Ba/Fe] = −0.4 dex. This particular abundance pattern was not explained by our previous models for neutron capture elements in the Galactic halo. In our previous work (Cescutti et al. 2013; Cescutti & Chiappini 2014), we showed that an r-process component and the spinstars contribution of s-process can account for most of the data in literature. We decide thus to include also a variation on the iron yields mimicking the production of iron by faint SNe. The final model, that we call spinning faint SNe, is able to explain the presence also of the most extreme stars in the [Ba/Fe] ratio vs. [Fe/H] space. The comparison of the model with the observational data also indicates that the r-process events are not linked to faint SNe events. Since most of the stars at such a low metallicity appear to be quite enhanced in carbon, we decided to show also the results of our model in the [C/Fe] ratio vs. [Fe/H] space. We find that the model is able to explain the chemistry of TYC 8442−1036−1 and also to recover a large fraction of the CEMP-no stars. However, a not negligible fraction still remains not explicable. A scenario to explain these super CEMP-no stars is that these stars have been formed (almost) entirely from the material ejected through winds by fast rotating massive stars (Meynet et al. 2010; Maeder & Meynet 2015).

Acknowledgements. This work was partially supported by the UK Science and Technology Facilities Council (grant ST/M000958/1). We thank the referee for comments that improved the clarity of this paper. GC thanks Lorenzo Monaco and Giacomo Beccari for the support during the execution of the observations. GC also thanks Raphael Hirschi for his useful suggestions, Marco Limongi for his comments on the iron production, Sean Ryan and Piercarlo Bonifacio for their advices on the section of data analysis.

[4] HE 0107−5240 (Christlieb et al. 2002), HE 1327−2326 (Frebel et al. 2005), HE 0557−4840 (Norris et al. 2007); the record is now held by SMSS J031300.36−670839.3 (Keller et al. 2014).

References

Aoki, W., Honda, S., Beers, T. C., et al. 2005, ApJ, 632, 611
Asplund, M., Grevesse, N., Sauval, A. J., & Scott, P. 2009, ARA&A, 47, 481
Beers, T. C. & Christlieb, N. 2005, ARA&A, 43, 531
Bergemann, M. & Cescutti, G. 2010, A&A, 522, A9
Bergemann, M. & Gehren, T. 2008, A&A, 492, 823
Cayrel, R., Depagne, E., Spite, M., et al. 2004, A&A, 416, 1117
Cescutti, G. 2008, A&A, 481, 691
Cescutti, G. & Chiappini, C. 2010, A&A, 515, A102
Cescutti, G. & Chiappini, C. 2014, A&A, 565, A51
Cescutti, G., Chiappini, C., Hirschi, R., Meynet, G., & Frischknecht, U. 2013, A&A, 553, A51
Cescutti, G., François, P., Matteucci, F., Cayrel, R., & Spite, M. 2006, A&A, 448, 557
Cescutti, G., Romano, D., Matteucci, F., Chiappini, C., & Hirschi, R. 2015, A&A, 577, A139
Chiappini, C., Ekström, S., Meynet, G., et al. 2008, A&A, 479, L9
Chiappini, C., Hirschi, R., Meynet, G., et al. 2006, A&A, 449, L27
Chieffi, A. & Limongi, M. 2013, ApJ, 764, 21
Christlieb, N., Bessell, M. S., Beers, T. C., et al. 2002, Nature, 419, 904
Cooke, R. J. & Madau, P. 2014, ApJ, 791, 116
Cristallo, S., Piersanti, L., Straniero, O., et al. 2011, ApJS, 197, 17
Cristallo, S., Straniero, O., Gallino, R., et al. 2009, ApJ, 696, 797
Dekker, H., D'Odorico, S., Kaufer, A., Delabre, B., & Kotzlowski, H. 2000, in Society of Photo-Optical Instrumentation Engineers (SPIE) Conference Series, Vol. 4008, Optical and IR Telescope Instrumentation and Detectors, ed. M. Iye & A. F. Moorwood, 534–545
Frebel, A., Aoki, W., Christlieb, N., et al. 2005, Nature, 434, 871
Frebel, A., Christlieb, N., Norris, J. E., et al. 2006, ApJ, 652, 1585
Frischknecht, U., Hirschi, R., Pignatari, M., et al. 2016, MNRAS, 456, 1803
Frischknecht, U., Hirschi, R., & Thielemann, F.-K. 2012, A&A, 538, L2
Fujimoto, M. Y., Ikeda, Y., & Iben, Jr., I. 2000, ApJ, 529, L25
Gustafsson, B., Edvardsson, B., Eriksson, K., et al. 2008, A&A, 486, 951

Hansen, C. J., Nordstroem, B., Hansen, T. T., et al. 2015a, ArXiv e-prints [arXiv:1511.07812]
Hansen, C. J., Primas, F., Hartman, H., et al. 2012, A&A, 545, A31
Hansen, T., Hansen, C. J., Christlieb, N., et al. 2015b, ApJ, 807, 173
Hill, V., Plez, B., Cayrel, R., et al. 2002, A&A, 387, 560
Hirschi, R. 2007, A&A, 461, 571
Janka, H.-T., Hanke, F., Hüdepohl, L., et al. 2012, Progress of Theoretical and Experimental Physics, 2012, 010000
Keller, S. C., Bessell, M. S., Frebel, A., et al. 2014, Nature, 506, 463
Komiya, Y., Suda, T., Minaguchi, H., et al. 2007, ApJ, 658, 367
Kupka, F. G., Ryabchikova, T. A., Piskunov, N. E., Stempels, H. C., & Weiss, W. W. 2000, Baltic Astronomy, 9, 590
Li, H. N., Christlieb, N., Schörck, T., et al. 2010, A&A, 521, A10
Lind, K., Asplund, M., Barklem, P. S., & Belyaev, A. K. 2011, A&A, 528, A103
Lind, K., Bergemann, M., & Asplund, M. 2012, MNRAS, 427, 50
Maeder, A. & Meynet, G. 1989, A&A, 210, 155
Maeder, A. & Meynet, G. 2015, A&A, 580, A32
Mashonkina, L. 2013, A&A, 550, A28
McWilliam, A. 1998, AJ, 115, 1640
McWilliam, A., Preston, G. W., Sneden, C., & Searle, L. 1995, AJ, 109, 2757
Merle, T., Thévenin, F., Pichon, B., & Bigot, L. 2011, MNRAS, 418, 863
Meynet, G., Ekström, S., & Maeder, A. 2006, A&A, 447, 623
Meynet, G., Hirschi, R., Ekstrom, S., et al. 2010, A&A, 521, A30
Meynet, G. & Maeder, A. 2002, A&A, 390, 561
Moriya, T., Tominaga, N., Tanaka, M., et al. 2010, ApJ, 719, 1445
Nishimura, N., Takiwaki, T., & Thielemann, F.-K. 2015, ArXiv e-prints [arXiv:1501.06567]
Nomoto, K., Tominaga, N., Umeda, H., Kobayashi, C., & Maeda, K. 2006, Nuclear Physics A, 777, 424
Norris, J. E., Christlieb, N., Korn, A. J., et al. 2007, ApJ, 670, 774
Osorio, Y. & Barklem, P. S. 2016, A&A, 586, A120
Pignatari, M., Gallino, R., Meynet, G., et al. 2008, ApJ, 687, L95
Placco, V. M., Frebel, A., Beers, T. C., & Stancliffe, R. J. 2014, ApJ, 797, 21
Prantzos, N. 2012, A&A, 542, A67
Roederer, I. U. 2013, AJ, 145, 26
Roederer, I. U., Cowan, J. J., Preston, G. W., et al. 2014a, MNRAS, 445, 2970
Roederer, I. U., Preston, G. W., Thompson, I. B., et al. 2014b, AJ, 147, 136
Ryan, S. G., Norris, J. E., & Beers, T. C. 1996, ApJ, 471, 254
Scalo, J. M. 1986, Fund. Cosmic Phys., 11, 1
Sneden, C., Cowan, J. J., Kobayashi, C., et al. 2015, ArXiv e-prints [arXiv:1511.05985]
Sousa, S. G., Santos, N. C., Israelian, G., Mayor, M., & Monteiro, M. J. P. F. G. 2007, A&A, 469, 783
Spite, M., Cayrel, R., Hill, V., et al. 2006, A&A, 455, 291
Spite, M., Cayrel, R., Plez, B., et al. 2005, A&A, 430, 655
Starkenburg, E., Shetrone, M. D., McConnachie, A. W., & Venn, K. A. 2014, MNRAS, 441, 1217
Thornton, K., Gaudlitz, M., Janka, H.-T., & Steinmetz, M. 1998, ApJ, 500, 95
Tominaga, N., Maeda, K., Umeda, H., et al. 2007, ApJ, 657, L77
Ural, U., Cescutti, G., Koch, A., et al. 2015, MNRAS, 449, 761
van den Hoek, L. B. & Groenewegen, M. A. T. 1997, A&AS, 123, 305
Winteler, C., Käppeli, R., Perego, A., et al. 2012, ApJ, 750, L22
Woosley, S. E. & Weaver, T. A. 1995, ApJS, 101, 181
Yong, D., Norris, J. E., Bessell, M. S., et al. 2013, ApJ, 762, 26

Table .1. Equivalent width for TYC 8442−1036−1.

Wavelength (Å)	Species	L.E.P. (eV)	log gf	W_λ (mÅ)
5889.951	Na I	0.000	0.112	89.11
5895.924	Na I	0.000	−0.191	69.92
4351.906	Mg I	4.340	−0.525	29.42
4702.990	Mg I	4.330	−0.380	43.16
5528.405	Mg I	4.340	−0.341	42.12
4283.011	Ca I	1.890	−0.220	22.29
4318.652	Ca I	1.900	−0.210	18.21
4425.437	Ca I	1.880	−0.360	15.01
4435.679	Ca I	1.890	−0.520	8.57
4454.779	Ca I	1.900	0.260	35.86
5265.556	Ca I	2.520	−0.260	5.54
5588.749	Ca I	2.520	0.210	12.43
5857.451	Ca I	2.930	0.230	4.99
6102.723	Ca I	1.880	−0.790	6.63
6122.217	Ca I	1.890	−0.320	17.35
6162.173	Ca I	1.900	−0.090	27.52
4246.822	Sc II	0.310	0.240	83.71
4314.083	Sc II	0.620	−0.100	46.27
4400.389	Sc II	0.610	−0.540	29.74
4415.557	Sc II	0.600	−0.670	23.33
5031.021	Sc II	1.360	−0.400	8.18
5526.790	Sc II	1.770	0.030	5.78
4533.241	Ti I	0.850	0.480	16.02
4534.776	Ti I	0.840	0.280	13.82
4981.731	Ti I	0.840	0.500	20.44
4991.065	Ti I	0.840	0.380	16.15
4999.503	Ti I	0.830	0.250	11.85
5014.276	Ti I	0.810	0.110	8.80
5039.957	Ti I	0.020	−1.130	4.20
5064.653	Ti I	0.050	−0.990	4.67
4290.219	Ti II	1.160	−0.930	56.93
4300.049	Ti II	1.180	−0.490	61.91
4337.915	Ti II	1.080	−0.980	53.50
4394.051	Ti II	1.220	−1.770	12.88
4395.033	Ti II	1.080	−0.510	73.55
4395.850	Ti II	1.240	−1.970	7.46
4399.772	Ti II	1.240	−1.220	38.05
4417.719	Ti II	1.160	−1.230	42.94
4418.330	Ti II	1.240	−1.990	6.96
4443.794	Ti II	1.080	−0.700	74.70
4444.558	Ti II	1.120	−2.210	10.41
4450.482	Ti II	1.080	−1.510	31.54
4464.450	Ti II	1.160	−1.810	15.35
4468.507	Ti II	1.130	−0.600	68.69
4470.857	Ti II	1.160	−2.060	7.40
4501.273	Ti II	1.120	−0.760	66.05
4533.969	Ti II	1.240	−0.540	67.72
4563.761	Ti II	1.220	−0.790	58.07
4571.968	Ti II	1.570	−0.230	57.79
4657.200	Ti II	1.240	−2.240	4.38
5129.152	Ti II	1.890	−1.300	6.00
5336.771	Ti II	1.580	−1.630	9.19
5381.015	Ti II	1.570	−1.970	5.72
4379.230	V I	0.300	0.550	5.11
4254.332	Cr I	0.000	−0.110	66.85
4274.796	Cr I	0.000	−0.230	60.79
4289.716	Cr I	0.000	−0.360	55.05
5409.772	Cr I	1.030	−0.720	6.65
4754.042	Mn I	2.280	-0.090	5.34
4823.524	Mn I	2.320	0.140	6.50

Wavelength (Å)	Species	L.E.P. (eV)	log gf	W_λ (mÅ)
4184.890	Fe I	2.830	−0.870	14.21
4187.039	Fe I	2.450	−0.550	47.95
4187.795	Fe I	2.420	−0.550	51.02
4191.431	Fe I	2.470	−0.730	37.05
4195.329	Fe I	3.330	−0.410	11.11
4199.095	Fe I	3.050	0.250	46.63
4202.029	Fe I	1.480	−0.700	86.50
4222.213	Fe I	2.450	−0.970	30.57
4227.427	Fe I	3.330	0.230	40.13
4233.603	Fe I	2.480	−0.600	40.67
4238.810	Fe I	3.400	−0.230	19.09
4250.119	Fe I	2.470	−0.400	50.75
4260.474	Fe I	2.400	−0.020	76.35
4271.154	Fe I	2.450	−0.350	57.11
4282.403	Fe I	2.170	−0.820	44.59
4337.046	Fe I	1.560	−1.700	43.97
4415.123	Fe I	1.610	−0.610	85.44
4430.614	Fe I	2.220	−1.660	12.55
4442.339	Fe I	2.200	−1.250	27.52
4447.717	Fe I	2.220	−1.340	25.53
4461.653	Fe I	0.090	−3.200	60.88
4466.552	Fe I	2.830	−0.600	30.33
4489.739	Fe I	0.120	−3.970	20.88
4494.563	Fe I	2.200	−1.140	35.54
4528.614	Fe I	2.180	−0.820	51.25
4531.148	Fe I	1.480	−2.150	26.30
4592.650	Fe I	1.560	−2.460	13.65
4602.940	Fe I	1.490	−2.210	26.46
4647.430	Fe I	2.950	−1.350	4.34
4871.318	Fe I	2.870	−0.360	35.08
4872.138	Fe I	2.880	−0.570	24.98
4891.492	Fe I	2.850	−0.110	49.26
4903.310	Fe I	2.880	−0.930	14.44
4918.994	Fe I	2.870	−0.340	36.83
4920.503	Fe I	2.830	0.070	55.96
4938.814	Fe I	2.870	−1.080	8.90
4939.687	Fe I	0.860	−3.340	14.13
4994.130	Fe I	0.920	−3.080	20.67
5001.864	Fe I	3.880	0.010	7.40
5006.119	Fe I	2.830	−0.620	23.36
5041.072	Fe I	0.960	−3.090	17.71
5041.756	Fe I	1.490	−2.200	24.04
5049.820	Fe I	2.280	−1.360	23.78
5051.635	Fe I	0.920	−2.800	32.09
5068.766	Fe I	2.940	−1.040	7.63
5079.740	Fe I	0.990	−3.220	12.20
5083.339	Fe I	0.960	−2.960	22.72
5110.413	Fe I	0.000	−3.760	41.65
5123.720	Fe I	1.010	−3.070	17.15
5127.359	Fe I	0.920	−3.310	10.90
5131.470	Fe I	2.220	−2.520	2.60
5254.955	Fe I	0.110	−4.760	4.74
5266.555	Fe I	3.000	−0.390	27.07
5269.537	Fe I	0.860	−1.320	106.40
5281.790	Fe I	3.040	−0.830	11.96
5283.621	Fe I	3.240	−0.520	13.52
5302.302	Fe I	3.280	−0.880	7.25
5307.361	Fe I	1.610	−2.990	4.02
5324.179	Fe I	3.210	−0.240	28.92
5328.039	Fe I	0.920	−1.470	97.30

Wavelength (Å)	Species	L.E.P. (eV)	log gf	W_λ (mÅ)
5328.532	Fe I	1.560	−1.850	42.70
5339.929	Fe I	3.270	−0.720	9.95
5367.470	Fe I	4.420	0.440	4.88
5369.962	Fe I	4.370	0.540	8.29
5371.490	Fe I	0.960	−1.650	91.01
5383.369	Fe I	4.310	0.640	15.37
5393.168	Fe I	3.240	−0.910	8.29
5397.128	Fe I	0.920	−1.990	78.19
5405.775	Fe I	0.990	−1.840	80.86
5410.910	Fe I	4.470	0.400	4.34
5415.200	Fe I	4.390	0.640	11.78
5429.697	Fe I	0.960	−1.880	82.44
5434.524	Fe I	1.010	−2.120	65.98
5446.917	Fe I	0.990	−1.910	77.60
5455.609	Fe I	1.010	−2.090	70.81
5497.516	Fe I	1.010	−2.850	26.69
5501.465	Fe I	0.960	−3.050	22.00
5506.779	Fe I	0.990	−2.800	29.13
5569.618	Fe I	3.420	−0.540	10.23
5572.842	Fe I	3.400	−0.310	15.23
5576.089	Fe I	3.430	−1.000	3.27
5586.756	Fe I	3.370	−0.140	21.36
5615.644	Fe I	3.330	−0.140	30.07
6065.480	Fe I	2.610	−1.410	9.84
6136.615	Fe I	2.450	−1.400	17.43
6137.692	Fe I	2.590	−1.400	12.11
4233.172	Fe II	2.580	−1.900	36.10
4416.830	Fe II	2.780	−2.410	7.66
4491.405	Fe II	2.860	−2.700	7.20
4508.288	Fe II	2.860	−2.250	13.71
4515.339	Fe II	2.840	−2.450	9.79
4520.224	Fe II	2.810	−2.600	8.70
4522.634	Fe II	2.840	−2.030	21.74
4541.524	Fe II	2.860	−2.790	4.39
4555.893	Fe II	2.830	−2.160	13.09
4576.340	Fe II	2.840	−2.820	3.84
5234.625	Fe II	3.220	−2.150	11.24
5476.900	Ni I	1.830	−0.890	40.62
4722.153	Zn I	4.030	−0.338	3.42
4810.528	Zn I	4.080	−0.137	3.57